Electronic structure and magnetism in UGa_2: DFT+DMFT approach

Banhi Chatterjee [1,2] and Jindřich Kolorenč [1,*]

[1] *Institute of Physics (FZU), Czech Academy of Sciences, Na Slovance 2, 182 21 Prague, Czech Republic*

[2] *Jožef Stefan Institute, Jamova 39, SI-1000 Ljubljana, Slovenia*

(Received 18 February 2021; revised 30 April 2021; accepted 7 May 2021; published 25 May 2021)

The debate whether uranium $5f$ electrons are closer to being localized or itinerant in the ferromagnetic compound UGa_2 is not yet fully settled. The experimentally determined magnetic moments are large, approximately $3\,\mu_B$, suggesting the localized character of the $5f$ electrons. In the same time, one can identify signs of itinerant as well as localized behavior in various spectroscopic observations. The band theory, employing local exchange-correlation functionals, is biased toward itinerant $5f$ states and severely underestimates the moments. Using material-specific dynamical mean-field theory (DMFT), we probe how a less approximate description of electron-electron correlations improves the picture. We present two variants of the theory: starting either from spin-restricted (LDA) or spin-polarized (LSDA) band structure. We show that the L(S)DA+DMFT method can accurately describe the magnetic moments in UGa_2 as long as the exchange interaction between the uranium $6d$ and $5f$ electrons is preserved by a judicious choice of the spin-polarized double-counting correction. We discuss the computed electronic structure in relation to photoemission experiments and show how the correlations reduce the Sommerfeld coefficient of the electronic specific heat by shifting the $5f$ states slightly away from the Fermi level.

DOI: 10.1103/PhysRevB.103.205146

I. INTRODUCTION

The $5f$ electrons in actinides and their compounds can be either itinerant and participating in chemical bonds, or localized and not contributing to cohesion. A transition akin to Mott metal–insulator transition occurs in elemental actinide metals between Pu and Am [1]. Although elemental uranium has itinerant $5f$ electrons, its compounds display both types of $5f$ states. A traditional way of classifying uranium compounds is by placing them in the Hill plot that relates the critical temperature (magnetic or superconducting) to the nearest neighbor U–U spacing [2]. Small U–U distances favor superconducting behavior at low temperatures, whereas long-range magnetic order takes place at spacings greater than the so-called Hill limit (3.5 Å).

In UGa_2, an intermetallic binary compound with a hexagonal AlB_2 structure (space group $P6/mmm$, Fig. 1), the Ga atoms effectively separate the uranium atoms, increasing the U–U distance to 4.0 Å, that is, above the Hill limit. Accordingly, the compound exhibits ferromagnetic order below $T_C = 125$ K with the easy magnetization axis along the [100] direction. Experimental observations establish magnetic moments of approximately $3\,\mu_B$ per U atom in the ferromagnetic phase, using magnetization measurements [3,4] as well as neutron diffraction [5,6]. UGa_2 thus exhibits moments and ordering temperature that are larger than typical for ferromagnetic uranium intermetallics [7], which indicates localized $5f$ electrons. The magnetic behavior can indeed be accurately reproduced by a fully local crystal-field model corresponding to the $5f^3$ configuration of the U ion [8]. In addition, the observed Sommerfeld coefficient $\gamma = 11$ mJ mol^{-1} K^{-2} [9] is not much enhanced compared to the analogous compound without $5f$ electrons, $LaGa_2$, displaying $\gamma = 4$ mJ mol^{-1} K^{-2} [10], which testifies against a high density of electronic states at the Fermi level in UGa_2, again favoring the localized picture of the $5f$ electrons. The spectroscopic evidence, on the other hand, is not conclusive about the nature of the $5f$ states since one can identify spectral features characteristic to localized electrons as well as features typical to itinerant electrons [11–13]. Similarly, the Fermi surface probed by the de Haas–van Alphen effect is not compatible with full $5f$ localization [9].

The large spin-orbit coupling (SOC), the crystal-field splitting, and the Coulomb interaction between the $5f$ electrons influence the magnetic moments in a nontrivial manner. This complexity contributes to the fact that the electronic structure of UGa_2 is not yet satisfactorily understood. The first-principles band theory based on semi-local approximations to the density-functional theory (DFT) severely underestimates the moments, yielding about $0.6\,\mu_B$ per uranium atom [14,15]. The correlated band theory incorporating an on-site Hubbard interaction term, DFT+U, can successfully model the magnetically ordered states, particularly in insulating compounds with localized 5f electrons [16–18]. In UGa_2, it enhances the magnetic moments up to $2.8\,\mu_B$ but the spectroscopic results are not reproduced very well [15,19].

The DFT+U method is a static mean-field approximation and as such it cannot account for the multi-reference character of the $5f$ shell nor for dynamical many-body effects. These limitations are lifted when DFT is combined with the dynamical mean-field theory (DMFT) [20,21], which accurately models both itinerant and localized electrons. In this paper, we investigate how the theoretical description of the magnetism

*kolorenc@fzu.cz

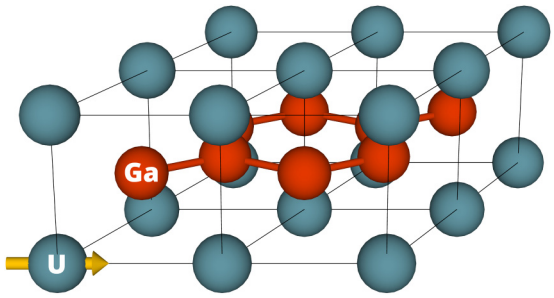

FIG. 1. The hexagonal lattice of UGa_2 with uranium atoms shown in blue and gallium atoms in red. The uranium magnetic moments (arrow) are aligned along the [100] direction.

and of the electronic structure of UGa_2 improves when the DFT+DMFT is applied. We estimate and discuss the effects of the $6d-5f$ exchange interactions on the $5f$ magnetic moments, and compare the computed spectral properties with the experimental valence-band photoemission spectra (PES). We also discuss technical matters pertaining to spin-polarized DFT+DMFT solutions.

II. METHOD

The DFT+DMFT method improves upon DFT+U by replacing the static mean-field potential, approximating the Coulomb interaction among the uranium $5f$ electrons, with an energy-dependent (dynamical) potential (self-energy) [20,22]. This self-energy is computed by solving an auxiliary impurity model—a many-body problem, for which we employ the exact diagonalization. We present two variants of the theory differentiated by the self-energy being inserted (a) into the spin-restricted LDA band structure (we call this method LDA+DMFT), and (b) into the ferromagnetic LSDA band structure (we refer to this variant as to LSDA+DMFT). A similar comparison of spin-restricted and spin-polarized parent band structures was performed for ferromagnetic nickel in Ref. [23].

A. General formalism

We start with determination of the first-principles band structure by means of the WIEN2K code [24] using parameters listed in Appendix A. Scalar relativistic effects as well as the spin-orbit coupling are included in these WIEN2K calculations [25]. Afterwards, the relevant valence bands are represented by a tight-binding Hamiltonian in the basis of the maximally-localized Wannier functions [26,27]. This Hamiltonian is then used as the parent band structure for the DMFT calculations.

In each iteration of the DMFT self-consistency cycle, the local electronic structure around one shell of the uranium $5f$ Wannier functions is mapped onto a noninteracting impurity model (Appendix B),

$$\hat{H}_{\mathrm{imp}} = \sum_{mm'\sigma\sigma'} [\mathbb{H}_{\mathrm{loc}}]^{\sigma\sigma'}_{mm'} \hat{f}^{\dagger}_{m\sigma} \hat{f}_{m'\sigma'} + \sum_{J} \epsilon_J \hat{b}^{\dagger}_J \hat{b}_J + \sum_{m\sigma J} (V_{Jm\sigma} \hat{f}^{\dagger}_{m\sigma} \hat{b}_J + V^{*}_{Jm\sigma} \hat{b}^{\dagger}_J \hat{f}_{m\sigma}), \quad (1)$$

where $\hat{f}^{\dagger}_{m\sigma}$ creates an electron in the $5f$ shell with magnetic quantum number m and spin projection $\sigma \in \{-1/2, 1/2\}$ (eigenvalues of $\hat{s}_z$). The first term in Eq. (1) corresponds to the local Hamiltonian, which describes the $5f$ shell. It can be decomposed as

$$\mathbb{H}_{\mathrm{loc}} = \epsilon_f \hat{I} + \zeta \hat{\mathbf{l}} \cdot \hat{\mathbf{s}} - \hat{\mathbf{s}} \cdot \mathbf{\Delta}_X + B_{20}\hat{O}_{20} + B_{40}\hat{O}_{40} + B_{60}\hat{O}_{60} + B_{66}\hat{O}_{66}, \quad (2)$$

where ϵ_f is the energy of the $5f$ level, ζ is the strength of the SOC, $\mathbf{\Delta}_X$ gives the exchange splitting, and $\hat{O}_{kq}$ and B_{kq} are Stevens operators and the corresponding parameters that characterize the D_{6h} crystal-field potential at the uranium site in UGa_2. In general, the parameters B_{kq} can be spin dependent, which we briefly discuss at the end of Appendix C. Note that the decomposition introduced in Eq. (2) is only used for the analysis of $\mathbb{H}_{\mathrm{loc}}$ and has no influence on the DMFT calculations and results.

The second term in Eq. (1) corresponds to an effective medium usually referred to as the bath, with which the $5f$ shell interacts. The operator $\hat{b}^{\dagger}_J$ creates an electron in this effective medium. The last term in Eq. (1) accounts for the hybridization of the $5f$ shell with the bath. In our calculations, the off-diagonal hybridization induced by the noncommutativity of the hexagonal symmetry with the SOC is fully taken into account. The crystal-field splitting of the $5f$ states is partly due to the crystal-field potential contained in $\mathbb{H}_{\mathrm{loc}}$ and partly due to the hybridization.

The full interacting impurity model, in which the self-energy is computed, is given by

$$\hat{H}^{\mathrm{DMFT}}_{\mathrm{imp}} = \hat{H}_{\mathrm{imp}} + \hat{U}, \quad (3)$$

where $\hat{H}_{\mathrm{imp}}$ is the noninteracting one-electron part shown in Eq. (1) and $\hat{U}$ is the Coulomb repulsion among the $5f$ electrons,

$$\hat{U} = \frac{1}{2} \sum_{\substack{mm'm''\\ m'''\sigma\sigma'}} U_{mm'm''m'''} \hat{f}^{\dagger}_{m\sigma} \hat{f}^{\dagger}_{m'\sigma'} \hat{f}_{m'''\sigma'} \hat{f}_{m''\sigma} - \sum_{m\sigma} (U_H - \sigma U_X) \hat{f}^{\dagger}_{m\sigma} \hat{f}_{m\sigma}, \quad (4)$$

where $U_{mm'm''m'''}$ is considered in its full spherically symmetric form parametrized by four Slater integrals $F_0 = 2.0$ eV, $F_2 = 7.09$ eV, $F_4 = 4.60$ eV, and $F_6 = 3.36$ eV, which correspond to Coulomb $U = 2.0$ eV and Hund $J = 0.59$ eV. The first integral, F_0, is at the upper limit, beyond which the $5f$ peak in the occupied LSDA+U density of states moves too far from the Fermi level to be compatible with the valence-band photoemission spectra [11,15]. The other three parameters (F_2, F_4, F_6) correspond to the atomic Hartree–Fock values calculated for the U^{3+} ion ($5f^3$ configuration) and then reduced to 80% to mimic screening [28,29]. Note that the unscreened ionic F_k values yield Hund $J = 0.79$ eV, which can be considered as the maximal value for the uranium $5f^3$ systems.

The second term in Eq. (4) is the double-counting correction introduced to remove the static mean-field approximation of the $5f-5f$ Coulomb interaction that is incorporated in the DFT band structure. We assume the double-counting correction to be spherically symmetric (neither U_H nor U_X depends

on the magnetic quantum number m), with $U_X = 0$ for the LDA band structure and $U_X \neq 0$ for the LSDA band structure. The numerical values of U_H and U_X are discussed later in Secs. II C and II D.

The impurity model, Eq. (3), is solved using the exact diagonalization (Lanczos) method [30,31] as implemented in our in-house code [32]. The size of the models, which can be solved by this method, is limited due to unfavorable scaling of the computational demands. The impurity models employed in this paper consist of 14 spinorbitals corresponding to the $5f$ shell and another 42 spinorbitals representing the bath. Of the bath states, $N_b^< = 14$ orbitals have ϵ_J below the Fermi level (they are nominally occupied) and $N_b^> = 28$ orbitals have ϵ_J above the Fermi level (they are nominally empty). Even these small models are too demanding unless we turn to a reduction of the many-body basis inspired by the work of Gunnarsson and Schönhammer [32,33]. A cutoff M is introduced for each N-electron Hilbert space $\mathcal{H}_N$, and the diagonalization is performed only in a subspace

$$\mathcal{H}_N^{(M)} = \{|f^{N-N_b^<-n+m}\, b^n\, \underline{b}^m\rangle,\ 0 \leqslant m+n \leqslant M\}. \quad (5)$$

In this notation, $f^{N-N_b^<-n+m}$ indicates $N - N_b^< - n + m$ electrons in the uranium $5f$ shell, b^n indicates n electrons in the bath orbitals above the Fermi level, and $\underline{b}^m$ means m holes in the bath orbitals below the Fermi level. We use $M = 2$ for the cutoff. The convergence with respect to M is discussed in Appendix D.

The impurity solver yields a self-energy $[\hat{\Sigma}(z)]^{\sigma\sigma'}_{mm'}$ acting in the subspace of 5f spinorbitals, which enters the Dyson equation for the local Green's function $\hat{G}(z)$,

$$\hat{G}(z) = \frac{1}{\mathcal{N}} \sum_{\mathbf{k}} [z\hat{I} - \hat{H}_{\mathbf{k}} - \hat{\Sigma}(z)]^{-1}, \quad (6)$$

where $\mathcal{N}$ is the number of k points in the Brillouin zone (4096 in our calculations) and $\hat{H}_{\mathbf{k}}$ is the tight-binding Hamiltonian. The local Green's function determines an updated impurity model (Appendix B), concluding one iteration of the DMFT cycle.

After the DMFT self-consistency is reached, the occupation matrix of the $5f$ states is evaluated from the $5f$ block of the local Green's function,

$$\hat{n}_f = \int_{-\infty}^{E_\mathrm{F}} \hat{A}_f(\epsilon)\, d\epsilon, \quad \hat{A}_f(\epsilon) = -\frac{1}{\pi} \operatorname{Im} \hat{G}_f(\epsilon + \mathrm{i}0), \quad (7)$$

where the integral runs over all occupied states up to the Fermi energy E_F. Knowing the occupation matrix, we can calculate the $5f$ electron occupation as well as spin and orbital moments as averages of the corresponding operators,

$$n_f = \operatorname{Tr}(\hat{n}_f) \quad \text{and} \quad \langle O \rangle = \operatorname{Tr}(\hat{O}\,\hat{n}_f). \quad (8)$$

Finally, the Sommerfeld coefficient of the electronic specific heat γ is evaluated using the Fermi-liquid formula

$$\gamma = \frac{\pi k_\mathrm{B}^2}{3} \left[\frac{g_f(E_\mathrm{F})}{Z_f} + g_{spd}(E_\mathrm{F}) \right], \quad (9)$$

where $g_f(E_\mathrm{F}) = \operatorname{Tr}[\hat{A}_f(E_\mathrm{F})]$ is the density of $5f$ states at the Fermi energy, $g_{spd}(E_\mathrm{F})$ is the density of all other states at the Fermi energy, and $Z_f < 1$ is the average quasiparticle weight in the $5f$ bands that is estimated from the DMFT self-energy as suggested in Ref. [34],

$$\frac{1}{Z_f} = \operatorname{Tr}\left[\frac{\hat{A}_f(E_\mathrm{F})}{g_f(E_\mathrm{F})} \left(\hat{I} - \frac{d\hat{\Sigma}(\epsilon + \mathrm{i}0)}{d\epsilon} \right) \Bigg|_{\epsilon = E_\mathrm{F}} \right]. \quad (10)$$

All DMFT calculations presented in this paper are performed at temperature $T = 0$ K in order to obtain the ferromagnetic state with saturated magnetic moments.

B. Choice of the tight-binding model

We investigated several tight-binding models $\hat{H}_{\mathbf{k}}$ of increasing size. As the minimal model, we considered one that contains gallium $4s$ and $4p$, and uranium $5f$ and $6d$ states. Then we included uranium $7s$ and finally also $7p$ states. Various characteristics of these models are listed in Table I. Although the uranium $7p$ states are relatively high above the Fermi level, their inclusion makes a sizable difference, in particular to the crystal-field parameters in $\mathbb{H}_{\mathrm{loc}}$ and to the filling of the gallium states.

On the top of that, we found that the LDA+DMFT calculations without the U $7p$ states converge to the out-of-plane [001] ferromagnetic state, whereas the calculations with the U $7p$ states predict an in-plane ferromagnetic state. Since the experiments determine UGa_2 to be an in-plane ferromagnet [3,4], all results presented in the following sections were obtained in the tight-binding models that include uranium $7s$ and $7p$ states.

C. LDA+DMFT

When the parent band structure is spin-restricted (LDA), we induce the ferromagnetic solution by introducing a small symmetry-breaking magnetic field into the impurity model, Eq. (1), in the first few iterations of the DMFT self-consistency cycle. Afterwards, this field is removed again. Since we do not implement any charge self-consistency, the tight-binding Hamiltonian $\hat{H}_{\mathbf{k}}$ remains unchanged during the whole LDA+DMFT cycle and the spin (and orbital) polarization is introduced only by means of the polarized self-energy applied to the $5f$ states. This method very likely results in an underestimated spin polarization of the $6d$ bands. Moreover, the local Hamiltonian $\mathbb{H}_{\mathrm{loc}}$ stays nonpolarized as demonstrated in Appendix C, that is, no exchange field $\mathbf{\Delta}_X$ is induced in $\mathbb{H}_{\mathrm{loc}}$ by the polarized self-energy. Nevertheless, there should be some exchange field present in $\mathbb{H}_{\mathrm{loc}}$ due to the partially filled and partially polarized $6d$ bands, and neglecting this exchange certainly means underestimated $5f$ moments (which is indeed what we observe in Sec. III A). We fix this deficiency by introducing an empirical exchange field $\mathbf{\Delta}_{fd}$ analogously to the earlier computational studies of rare-earth systems [35,36]. The magnitude of this field is estimated as $\Delta_{fd} \approx I_{fd} m_d$ [35], where m_d is the magnetic moment due to the $6d$ electrons and I_{fd} is intra-atomic exchange integral. The magnetic moment is approximated by its LSDA value, $m_d \approx 0.24\ \mu_\mathrm{B}$ (see Table I for the spin-resolved filling of the $6d$ bands), the exchange integral is estimated by atomic calculations, $I_{fd} \approx 0.15$ eV/μ_B [37]. This yields $I_{fd} m_d \approx 36$ meV and we explore the LDA+DMFT solutions for Δ_{fd} varied around this value.

TABLE I. Characteristics of several tight-binding models derived from the DFT band structure. All models contain gallium $4s$ and $4p$ orbitals, the included uranium orbitals are listed in the first column. The quantities ζ, ϵ_f, and Δ_X are shown in eV, the crystal-field parameters B_{kq} in meV.

	Orbital occupations									Local Hamiltonian $\mathbb{H}_{\text{loc}}$						
Model	U $5f$	U $5f\uparrow$	U $5f\downarrow$	U $6d\uparrow$	U $6d\downarrow$	U $7s$	U $7p$	Ga $4s$	Ga $4p$	ζ	ϵ_f	Δ_X	B_{20}	B_{40}	B_{60}	B_{66}
Nonmagnetic solution																
d, f	2.79			0.94	0.94	–	–	1.51	2.18	0.248	0.634	0	−0.72	−0.14	0.00	−0.19
s, d, f	2.77			0.95	0.95	0.35	–	1.50	2.03	0.248	0.639	0	−0.69	−0.12	−0.01	−0.16
s, p, d, f	2.72			1.03	1.03	0.76	0.74	1.39	1.50	0.251	0.679	0	−2.83	−0.01	0.00	−0.06
Ferromagnetic solution [001]																
s, d, f	2.77	2.41	0.37	1.00	0.87	0.35	–	1.49	2.02	0.246	0.926	0.972	5.98	−0.11	−0.01	−0.16
s, p, d, f	2.72	2.37	0.36	1.08	0.96	0.76	0.74	1.39	1.49	0.249	0.968	0.980	3.71	0.01	0.00	−0.05
Ferromagnetic solution [210]																
s, p, d, f	2.72	2.34	0.38	1.08	0.95	0.76	0.74	1.34	1.54	0.248	0.956	0.956	3.92	0.03	0.00	−0.04

The absence of $\mathbf{\Delta}_X$ is a disadvantage of the spin-restricted parent band structure. Its advantage, on the other hand, is that the double-counting correction in Eq. (4) reduces to a single number U_H, since the spin-dependent part U_X vanishes. One possible approximation to the double counting is the so-called fully localized limit (FLL),

$$U_H^{\text{FLL}} = U(n_f - 1/2) - J(n_f - 1)/2, \tag{11}$$

where n_f is the self-consistently determined number of $5f$ electrons [16,38]. In our calculations, it turned out that this U_H^{FLL} severely overestimates the number of $5f$ electrons, resulting in $n_f \approx 4$. We hence employ an alternative strategy: we choose U_H such that the number of $5f$ electrons remains close to its LDA value ($n_f = 2.72$, Table I) also in the LDA+DMFT solution to simulate charge self-consistency [39,40]. This condition implies $U_H \approx 3$ eV. We note in passing that the FLL formula, Eq. (11), gives 3.93 eV for $n_f = 2.72$, 4.41 eV for $n_f = 3$, and 2.71 eV for $n_f = 2$.

D. LSDA+DMFT

As discussed above, using spin-restricted LDA as the parent band structure has two deficiencies: underestimated spin polarization of the $6d$ (and other) bands, and missing exchange field due to $6d$ moments acting on the $5f$ electrons. We dealt with the second issue empirically, but we did not address the first one yet. We attempt to do so by using the spin-polarized (LSDA) solution as the parent band structure. This way, all non-$5f$ bands are potentially spin-polarized, which enhances the polarization of the bath and of the bath–$5f$ hybridization in the auxiliary impurity model, Eq. (1), when compared to LDA+DMFT described in Sec. II C.

Although it may seem that the LSDA parent band structure also provides an improved estimate of the local exchange field $\mathbf{\Delta}_X$, it is not so, since the LSDA exchange field combines the $6d$–$5f$ exchange (tens of meV) with the $5f$–$5f$ exchange (about 1 eV). The latter has to be removed by the double-counting correction U_X, which we know only approximately. The FLL ansatz for the double counting U_X reads as [16]

$$U_X^{\text{FLL}} = E_{\text{FLL}}^{\downarrow} - E_{\text{FLL}}^{\uparrow} = J(n_f^{\uparrow} - n_f^{\downarrow}), \tag{12}$$

where

$$E_{\text{FLL}}^{\sigma} = U(n_f - 1/2) - J(n_f^{\sigma} - 1/2), \tag{13}$$

which we find to overcorrect the LSDA $5f$–$5f$ exchange. With the LSDA occupation numbers (Table I) and with $J = 0.59$ eV, the double counting U_X^{FLL} becomes 1.19 eV, whereas the LSDA exchange is only $\Delta_X = 0.98$ eV (Table I).

Instead of using Eq. (12) or any other similar formula, we again employ the approach introduced in Sec. II C, that is, we select U_X such that $\Delta_{fd} = \Delta_X - U_X \approx I_{fd} m_d \approx 36$ meV. Since Δ_X is a parameter of the local Hamiltonian, it remains constant during the DMFT self-consistency iterations as follows from the derivation presented in Appendix C, hence Δ_{fd} and U_X remain constant as well.

For the spin-independent part of the double-counting correction, we choose $U_H = 3.3$ eV. This value is 0.3 eV larger than in LDA+DMFT because the average position of the $5f$ level is approximately 0.3 eV higher in the ferromagnetic LSDA solution compared to the nonmagnetic LDA solution (Table I).

III. RESULTS

A. Magnetic moments

The method outlined in the preceding sections is not entirely self-contained—there are several semiempirical parameters, such as the Coulomb parameters F_k, the double-counting correction U_H, and the exchange field Δ_{fd}. Especially the exchange field was estimated only roughly and hence we decided to explore a range of values around this estimate.

In Fig. 2, we show how the magnetic moments depend on Δ_{fd} in the LDA+DMFT calculations when Δ_{fd} is applied in plane, along the [210] direction, which corresponds to the [210] ferromagnetic state.[1] The orbital and spin contributions to the magnetic moment are antiparallel as expected for $5f$

[1]We choose the [210] in-plane direction of magnetization instead of the experimental [100] direction due to technical limitation of our impurity solver. We have checked that this change does not significantly affect the ordered magnetic moments or the spectra in LSDA (Table III).

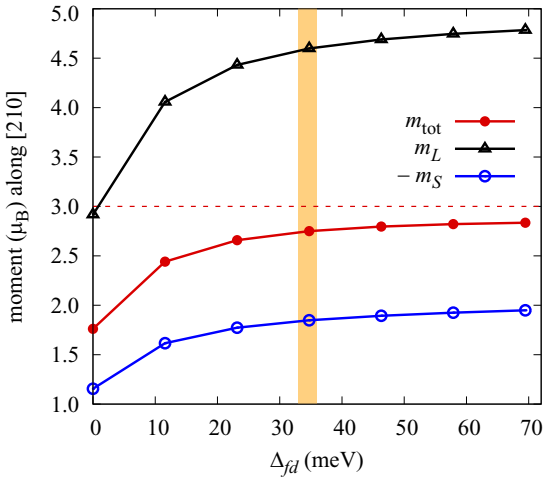

FIG. 2. The total magnetic moment (red), the orbital (black) and spin (blue) contributions to the magnetic moment of the $5f$ shell as functions of the exchange field Δ_{fd} applied along the [210] direction in the LDA+DMFT calculations. The realistic value of Δ_{fd} is marked by the orange stripe, the experimental magnetic moment is indicated by the dashed line [4].

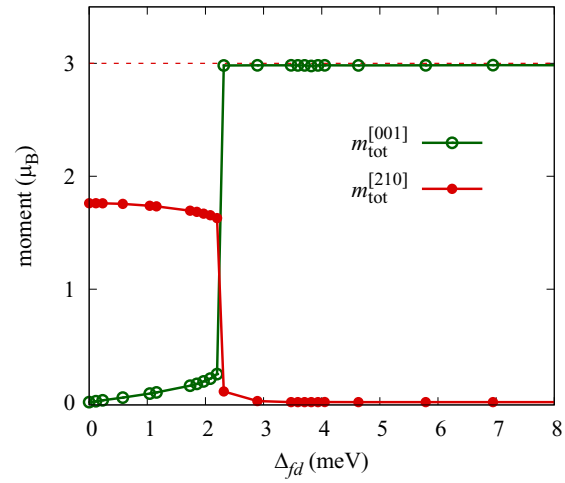

FIG. 3. Projection of the total magnetic moment to the [210] direction (red) and to the [001] direction (green) when the exchange field Δ_{fd} is applied along the [001] direction and the LDA+DMFT calculations are started from the LDA solution with $\Sigma(z) = 0$. The orbital and spin moments (not shown) behave similarly as in Fig. 2.

filling smaller than 7. At $\Delta_{fd} = 0$ meV, the total magnetic moment is clearly underestimated (1.76 μ_B), which confirms our earlier reasoning that some exchange field has to be introduced. As the exchange field increases, the magnetic moment quickly increases too, it reaches 2.75 μ_B at $\Delta_{fd} = 35$ meV, at which point it is already very close to the saturation value $\approx$2.88 μ_B. The quick saturation of the moments is a convenient feature—an inaccuracy in estimating the realistic value of Δ_{fd} translates to only a minor uncertainty of the computed magnetic moments. The moments and $5f$ filling at the realistic value of Δ_{fd} are compared to the LSDA solution and to experiments in Table II.

Analogous calculations were performed also for the exchange field Δ_{fd} applied along the out-of-plane [001] direction. In this case, the ferromagnetic state parallel to the exchange field is stable only above some critical value of Δ_{fd}, see Fig. 3. Above this value, the magnetic moment very quickly saturates, much faster that in Fig. 2. For smaller values of Δ_{fd}, the DMFT iterations converge to a nearly in-plane state with just a small out-of-plane tilt of the magnetic moments. For a range of Δ_{fd} values, we get two stationary solutions, one nearly in-plane and the other out-of-plane, depending on the starting point of the DMFT iterations. Figure 3 shows calculations that were started at a given Δ_{fd} from the LDA state with $\Sigma(z) = 0$. The transition from the in-plane to out-of-plane state then occurs at $\Delta_{fd} \approx 2.2$ meV. Calculations starting from the [001] ferromagnetic state converge to the out-of-plane state already at $\Delta_{fd} \gtrsim 0.6$ meV (not shown).

Unfortunately, we cannot determine which of the two stationary states found for Δ_{fd} between 0.6 and 2.2 meV is the ground state because we cannot reliably evaluate the total energy in our LDA+DMFT implementation. For the same reason, we cannot estimate the magnetocrystalline anisotropy energy. We can, however, conclude that the response of the magnetic moments to Δ_{fd} as observed in LDA+DMFT is consistent with the experimental finding that the easy axis is oriented in plane. Starting from the paramagnetic state ($\Delta_{fd} = 0$) and cooling down, the system always ends up in the in-plane state, since the moments exhibit an instability toward in-plane direction. Increasing in-plane moment increases in-plane Δ_{fd}, which stabilizes the in-plane state further.

The magnetic moments computed using LSDA+DMFT, with the spin-dependent part of the double-counting correction U_X varied to reproduce the same range of Δ_{fd} as explored above, are presented in Figs. 4 and 5 for the in-plane and out-of-plane orientations of the LSDA polarization. As in the LDA+DMFT, the total magnetic moments relatively quickly saturate with increasing Δ_{fd}, and the saturation is again faster in the [001] state than in the [210] state. Surprisingly, the saturated values of the total moments are noticeably smaller than in the corresponding LDA+DMFT calculations, by 15% in the case of the [210] ferromagnet and by 30% in the case of the

TABLE II. The orbital and spin magnetic moments in uranium $5f$ shells, m_S and m_L (in μ_B), the total magnetic moment in the unit cell m_{tot} (in μ_B), the occupation of the $5f$ shells n_f, and the Sommerfeld coefficient γ (in mJ mol^{-1} K^{-2}). The moments and the $5f$ filling correspond to the maximally localized Wannier functions. The experimental m_{tot} is taken from Ref. [4], the experimental γ from Ref. [9].

	U_H	Δ_{fd}	dir.	m_S	m_L	m_{tot}	n_f	γ
LSDA	–	–	[210]	−1.96	2.79	0.65	2.72	24.5
LSDA	–	–	[001]	−2.00	2.89	0.70	2.72	21.2
LDA+DMFT	3.0	35	[210]	−1.85	4.60	2.75	2.76	8.2
LDA+DMFT	3.0	35	[001]	−1.91	4.87	2.96	2.74	7.7
LSDA+DMFT	3.3	35	[210]	−1.66	4.15	2.30	2.82	7.2
LSDA+DMFT	3.3	35	[001]	−1.59	3.89	2.12	2.80	7.5
Experiment						3.07		11.0

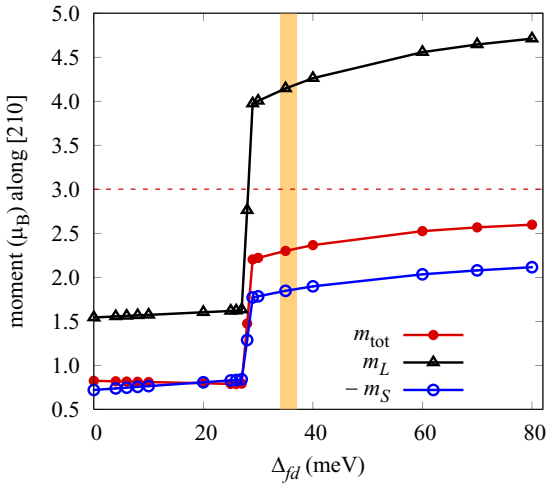

FIG. 4. Variation of magnetic moments with Δ_{fd}, computed using the LSDA+DMFT method when the parent band structure is polarized in the [210] direction. Compare with Fig. 2.

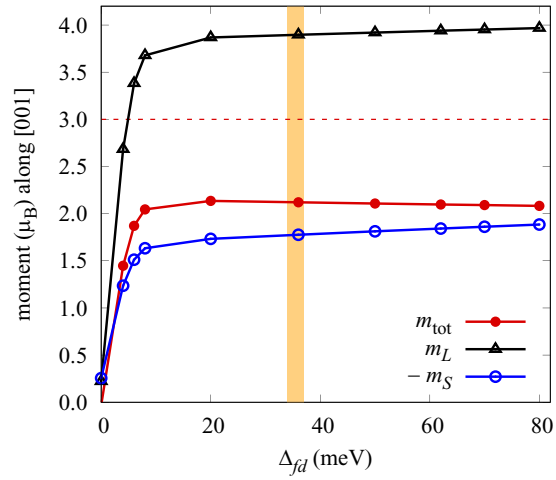

FIG. 5. The same plot as in Fig. 4, only the parent LSDA band structure is polarized in the [001] direction. To be compared with Fig. 3.

[001] ferromagnet (compare with Figs. 2 and 3). We expected the opposite, since the LSDA parent band structure is certainly more polarized than the LDA parent band structure—besides Δ_{fd} that is the same in both approaches by construction, the LSDA has all non-$5f$ bands spin split, which results in an enhanced polarization of the hybridization function. Intuitively, this should have induced a larger polarization in the $5f$ shell but the calculations show that it does not.

The difference in the computed moments could in principle be due to a difference in fillings of the $5f$ shell between the LDA+DMFT and LSDA+DMFT solutions, but this is not the case either. The $5f$ filling in both methods is very close as can be checked in Table II where we summarize our results for the realistic setting of the exchange field Δ_{fd}. We speculate that the inaccurate LSDA+DMFT moments come from some artifact of the static LSDA approximation, possibly from an artificially broken symmetry. One suspect feature is the strong spin dependence of the crystal-field parameters B_{kq} in the local Hamiltonian shown in Appendix C. Another feature, for which we do not have a clear explanation and which is likely to be connected to the LSDA solution as well, is the jump in magnetic moments near $\Delta_{fd} = 30$ meV in Fig. 4.

Figures 3 show the computed magnetic moments as functions of the exchange field Δ_{fd} for a fixed spin-independent part of the double-counting correction U_H. Although the employed values of U_H are well justified in Secs. II C and II D, it is useful to analyze the sensitivity of the magnetic moments to changes of U_H or, equivalently, to changes of the $5f$ filling n_f. This sensitivity is illustrated in Fig. 6 for the [210] ferromagnetic state calculated with the LDA+DMFT method. The [001] ferromagnetic state and the results of the LSDA+DMFT method behave analogously. The magnetic moments increase toward the experimentally determined value with increasing n_f but this route to improved agreement with experiments does not have a solid physical backing. Moreover, it would come at the cost of worsened agreement with the spectroscopic measurements, since increased U_H would push the uranium $5f$ states to too large binding energies.

B. Valence-band spectroscopy

Two measurements of valence-band photoemission spectra of UGa_2 can be found in the literature, the ultraviolet photoemission spectrum [11] (UPS, shown in the left panel of Fig. 7) and the soft-x-ray photoemission spectrum [12] (SX-PES, shown in the middle panel of Fig. 7). The UPS was measured on sputter-deposited films at room temperature, that is, in the paramagnetic phase. The maximum intensity was observed just below the Fermi level with a long tail extending toward higher binding energies. The SX-PES was measured on a freshly cleaved single crystal at $T = 20$ K, that is, well below the Curie temperature. The spectrum shows a narrow peak slightly below the Fermi level accompanied with two

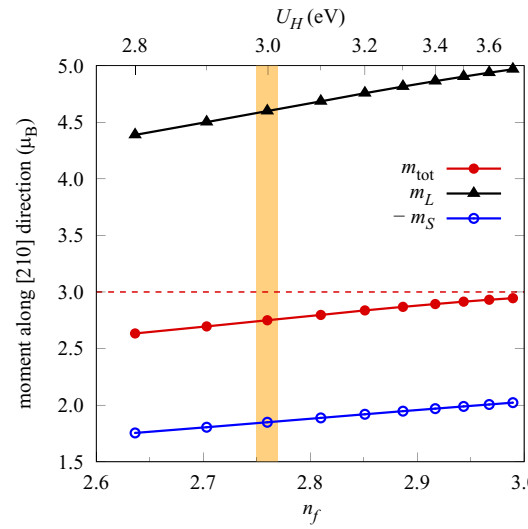

FIG. 6. The computed LDA+DMFT magnetic moments plotted as functions of the $5f$ filling n_f that is varied by changing the double-counting correction U_H. The exchange field $\Delta_{fd} = 35$ meV was applied along the [210] direction. The value $U_H = 3.0$ eV employed throughout the paper is marked by the orange stripe.

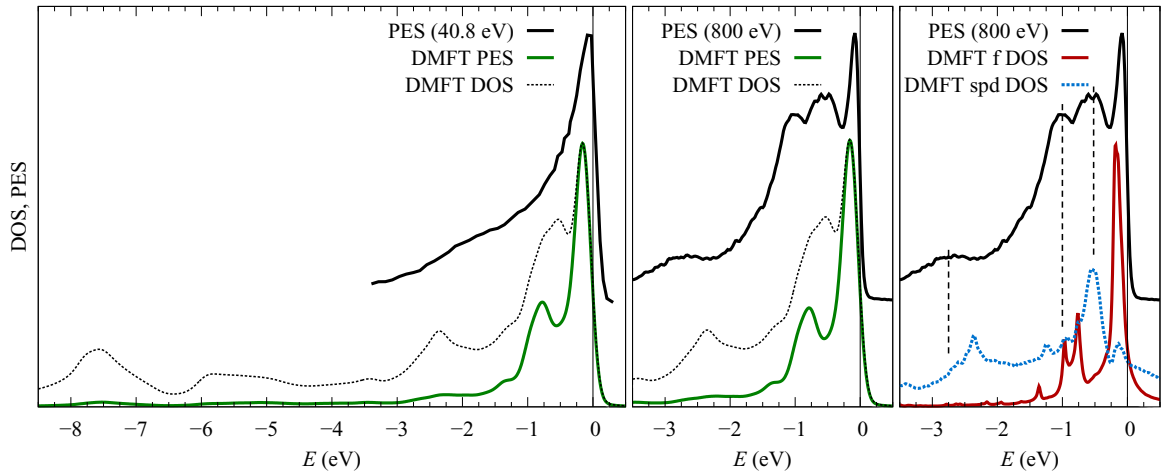

FIG. 7. Experimental photoelectron spectra (black line) from [11] (left) and from [12,41] (middle) are compared to the LDA+DMFT estimate of the spectra (green line). A Gaussian broadening (FWHM 0.2 eV) is added to simulate the instrument resolution. The LDA+DMFT total DOS, subject to the same broadening, is shown for comparison (dotted line). In the right panel, we plot the orbital-resolved DOS without broadening ($5f$ in red, sum of all others in dotted blue). All theoretical lines correspond to the [210] ferromagnet ($\Delta_{fd} = 35$ meV).

broader features at -0.5 and -1.0 eV, and an even broader hump can be discerned at -2.8 eV.

The two spectra are clearly different and the difference cannot be ascribed to the lower resolution of the UPS spectra. The magnetic order is also unlikely to cause such large changes, we certainly do not see any evidence of that in DFT+DMFT calculations (not shown), and the experiment does not detect any changes either [12]. The more probable source of the differences is the probing depth of the two experiments. The UPS used incident photons with energy 40.8 eV (He II line), SX-PES used 800 eV (synchrotron radiation), and hence the photoelectrons are emitted from deeper layers in the bulk of the sample in the SX-PES measurements.

Since our calculations do not include any surface effects, they should be closer to the SX-PES data. In Fig. 7, we show our theoretically estimated photoelectron spectra at the appropriate photon energies, calculated for the [210] ferromagnetic phase with the LDA+DMFT method ($\Delta_{fd} = 35$ meV, but the spectra are not sensitive to variations of the $6d-5f$ exchange field). The spectra are constructed as linear combinations of the *orbital-resolved* densities of states (DOS) weighted with photoionization cross sections listed in Ref. [42]. According to these cross sections, the $5f$ DOS has by far the largest weight for both 40.8 eV and 800 eV photon energies, and hence these photoemission measurements probe mainly the $5f$ states.

The computed spectra display a main peak at -0.15 eV and a satellite at -0.8 eV. The satellite has a considerably smaller intensity than the features seen in the SX-PES and as such the theory appears to be closer to the UPS spectra. The -0.5-eV and -2.8-eV features observed in SX-PES do not show up in the theoretical PES, but there are distinct peaks appearing at nearby energies in the LDA+DMFT *total* DOS (Fig. 7). They originate from orbitals that have small photoionization cross sections. These peaks are due to hybridized U $6d$ and Ga $4p$ bands at -0.5 eV, and mainly Ga $4p$ bands at -2.4 eV. The distinct feature outside the range probed by photoemission, at -7.6 eV, is due to Ga $4s$. The fact that SX-PES sees a signal where the theory places Ga $4p$ bands may be an indication that the theory underestimates the hybridization between Ga $4p$ and U $5f$ states. If the hybridization was stronger, some U $5f$ DOS would possibly appear at the position of the Ga $4p$ states, but that is just a speculation at this point.

Photoemission experiments access only the occupied part of the spectrum. The unoccupied part could be probed by inverse photoemission (we are not aware of any such experiment being performed to date) or by x-ray absorption spectroscopy (we discuss recent x-ray absorption measurements at the uranium $M_{4,5}$ edges in UGa_2 elsewhere [13]). In Fig. 8, we analyze the complete (occupied and unoccupied) $5f$ DOS from a theoretical perspective. We compare the LDA+DMFT result with the DOS computed for a spherically symmetric $5f^3$ ion,

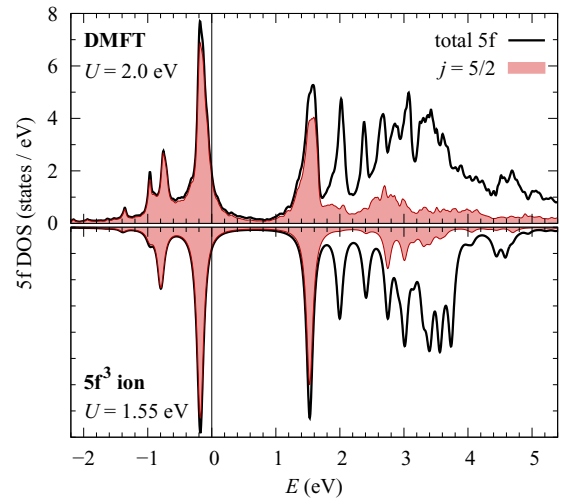

FIG. 8. The uranium $5f$ DOS in the [210] ferromagnet from the LDA+DMFT method ($\Delta_{fd} = 35$ meV) in the top panel is compared to the DOS from an atomic calculation ($5f^3$ state) in the bottom panel (black lines). The parameter $F_0 = U$ was reduced in the atomic calculation to mimic the screening effects incorporated in the LDA+DMFT method. The $j = 5/2$ components of the $5f$ DOS are shown in red.

since three is the closest integer value to the computed average $5f$ filling n_f (Table II) and the probability of finding the $5f$ shell in the $5f^3$ configuration predicted by LDA+DMFT is large, namely 83%. See Appendix D, Eq. (D1), for the meaning of the fluctuating number of $5f$ electrons. We can achieve a very close correspondence of the ionic and LDA+DMFT densities of states when the Coulomb U in the ionic model is reduced to 1.55 eV compared to 2.0 eV in LDA+DMFT. The higher Slater parameters F_k and the spin-orbit parameter ζ are identical. This observation indicates that the $5f$ states in the LDA+DMFT are very close to being fully localized, only their Coulomb repulsion is screened more than it would be in the fully localized Hubbard-I approximation. In addition, Fig. 8 also shows the $j = 5/2$ component of the $5f$ DOS to be compared with the shape of the M_4 absorption line [13].

Finally, in Fig. 9, we present the momentum-resolved $5f$ spectral density along high-symmetry directions in the Brillouin zone. We compare different models for the electronic correlations, namely LSDA, LSDA+U, and LSDA+DMFT, in the ferromagnetic state with magnetic moments pointing along the [210] direction. The [001] ferromagnetic state differs only in minor details. When the Hubbard term is included (LSDA+U and LSDA+DMFT), a gap between the occupied and unoccupied $5f$ bands appears and the occupied $5f$ states move slightly away from the Fermi level. Given the same interaction parameters (U and J, or F_k), this gap is larger in LSDA+U, which indicates that the screening of the Coulomb parameters is stronger in LSDA+DMFT than in LSDA+U. The situation is analogous to Fig. 8 since the U-induced potential in LSDA+U has the form of a ionic Hartree–Fock approximation. Another difference between the LSDA+DMFT and LSDA+U electronic structure is the incoherent character of the $5f$ states visible in the LSDA+DMFT solution, starting approximately 2.5 eV above the Fermi level.

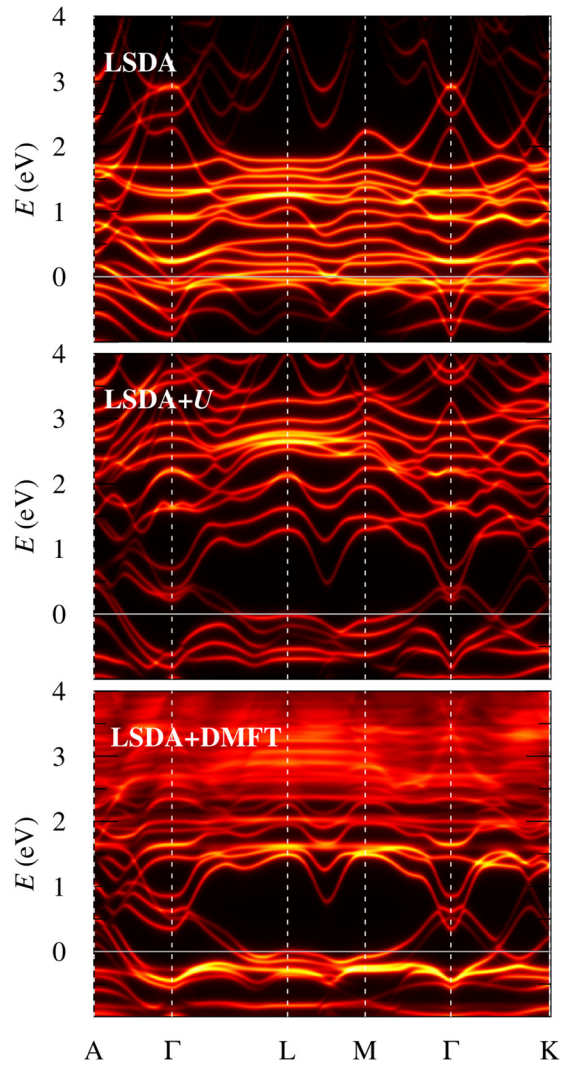

FIG. 9. Momentum-resolved $5f$ spectral density. The electronic correlations are described with increasing level of sophistication from top to bottom: LSDA, LSDA+U ($U = 2.0$ eV, $J = 0.59$ eV and the FLL double counting), and LSDA+DMFT (the same interaction parameters, and $U_H = 3.3$ eV and $\Delta_{fd} = 35$ meV). The [210] ferromagnetic state is shown in all three panels. The same U and J produce a larger gap between the occupied and unoccupied $5f$ states in LSDA+U than in LSDA+DMFT.

C. Sommerfeld coefficient

Figure 9 illustrates that the Fermi level cuts right through the $5f$ bands in LSDA, which is accompanied by a high density of states at the Fermi level and, subsequently, by a large Sommerfeld coefficient of the electronic specific heat γ. Indeed, LSDA predicts $\gamma > 20$ mJ mol^{-1} K^{-2} (Table II), which is at odds with the experimental value 11 mJ mol^{-1} K^{-2} [9]. In DFT+DMFT (and in LSDA+U as well), the $5f$ states move away from the Fermi level toward higher binding energies and the coefficient γ is reduced to approximately 8 mJ mol^{-1} K^{-2} (Table II), yielding a considerably better agreement with experiments. The computed Sommerfeld coefficient should be smaller than observed in experiments since we do not take into account any enhancement due to phonons. We do not observe much variation of γ when changing the orientation of the magnetic moments or when alternating the parent band structure (Table II).

IV. CONCLUSIONS

We have studied the electronic structure and magnetic properties of the ferromagnetic compound UGa_2 using the DFT+DMFT method, and compared our results with more approximate electronic-structure methods. We have found that our implementation of the DFT+DMFT method reproduces the experimentally observed large magnetic moments as well as the sign of the magnetocrystalline anisotropy energy, when the exchange interaction between uranium $6d$ and $5f$ states is included in a semiempirical manner. This is done either in the form of an extra potential acting on the $5f$ states or in the form of a spin-polarized double-counting correction. We have compared two formulations of the DFT+DMFT method, one keeping the non-$5f$ states spin restricted (LDA), and the other allowing their spin polarization (LSDA). Of the two, the LDA-based variant was found to provide more consistent results. It is a future work to investigate how the semiempirical approach to the $6d$–$5f$ exchange could be improved toward a fully first-principles method.

Besides the magnetic properties, we have also modeled the valence-band photoemission spectra on the basis of the DFT+DMFT density of states. We were not able to fully explain the differences between the two published photoemission experiments [11,12] but we could understand how the electron-electron correlations move the $5f$ states slightly away from the Fermi level, which is in accord with both photoemission spectra as well as with the observed small Sommerfeld coefficient of the electronic specific heat. With the aid of the DFT+DMFT method, it is thus possible to reconcile large magnetic moments and a small Sommerfeld coefficient with the $5f$ spectral density in the close vicinity of the Fermi level.

Our calculations indicate a close-to-localized uranium $5f$ states in UGa_2. From the comparison to the experimental photoemission spectra we deduce that the tendency to localization is probably slightly overestimated in our theoretical description. Such a tendency is to be expected for the employed impurity solver that implements a form of expansion around the atomic limit.

ACKNOWLEDGMENTS

The work was supported by the Czech Science Foundation under the Grants No. 18-02344S and 21-09766S. We thank S.-i. Fujimori for experimental data, and L. Havela, J. Kuneš and A. B. Shick for fruitful discussions. Computational resources were partially supplied by the project "e-Infrastruktura CZ" (e-INFRA LM2018140) provided within the program Projects of Large Research, Development and Innovations Infrastructures.

APPENDIX A: PARAMETERS OF DFT CALCULATIONS

To perform all DFT calculations presented in this paper, we employed the WIEN2K package [24] that implements linearized augmented plane-wave method and its extensions. It combines a scalar-relativistic description with spin-orbit coupling [25]. All calculations were performed at the experimental lattice constants $a = 4.213$ Å and $c = 4.020$ Å, reported in Ref. [3], with the following parameters: the radii of the muffin-tin spheres were $R_{\mathrm{MT}}(\mathrm{U}) = 2.80\,a_{\mathrm{B}}$ for uranium atoms and $R_{\mathrm{MT}}(\mathrm{Ga}) = 2.25\,a_{\mathrm{B}}$ for gallium atoms, the Brillouin zone was sampled with 6137 k points (900 k points in the irreducible wedge), and the basis-set cutoff $K_{\max}$ was defined with $R_{\mathrm{MT}}(\mathrm{Ga}) \times K_{\max} = 10.0$. The default basis set with local orbitals for semicore states (U $6s$, $6p$, and Ga $3d$) was used in all cases.

In Table III, we list the orbital and spin magnetic moments of the uranium $5f$ shell, the total magnetic moment of the unit cell, the filling of the $5f$ shell, and the Sommerfeld coefficient for three ferromagnetic states with moments pointing along different crystallographic axes. The moments and the filling of the $5f$ shell correspond to the muffin-tin sphere, they can be compared to the values computed for the maximally localized Wannier functions shown in Table II. The largest components of the total moment quoted in Table III are the $5f$ moments, a sizable contributions come also from the spin moments in the U $6d$ states ($\approx -0.1\ \mu_{\mathrm{B}}$) and in the interstitial ($\approx -0.2\ \mu_{\mathrm{B}}$). The moments induced at Ga atoms are negligible.

TABLE III. The orbital and spin magnetic moments in uranium $5f$ shell, m_S and m_L (in μ_{B}), the total magnetic moment in the unit cell m_{tot} (in μ_{B}), the occupation of the $5f$ shell n_f, and the Sommerfeld coefficient γ (in mJ mol^{-1} K^{-2}). The $5f$ magnetic moments and the $5f$ filling correspond to the atomic (muffin-tin) spheres.

	Direction	m_S	m_L	m_{tot}	n_f	γ
LDA	–	–	–	–	2.45	43.9
LSDA	[100]	−1.82	2.67	0.57	2.51	24.7
LSDA	[210]	−1.82	2.64	0.54	2.50	26.7
LSDA	[001]	−1.86	2.72	0.57	2.50	22.5

The maximally localized Wannier functions for the DMFT calculations were found with the WANNIER90 code [27]. The spread minimization was performed on $16 \times 16 \times 16$ mesh of k points. Since there are no gaps in the spectrum above the Fermi level, disentanglement was necessary [43]. We used 62 Bloch states on input, which corresponds to the energy window from −10 to 24 eV. (Our largest tight-binding models, that is, those actually used for the DMFT calculations, have 48 Wannier functions). The frozen inner window extended to 6 eV (3 eV for the smallest model listed in Table I), going higher meant that the centers of the Wannier functions started drifting away from the atomic centers, which is undesirable in our application that assumes the Wannier functions to be atomic-like. In the model used for the DMFT calculations, the original WIEN2K bands were represented perfectly up to 6 eV above the Fermi level, the match was still very good up to approximately 12 eV, and above that the correspondence quickly deteriorated.

APPENDIX B: CONSTRUCTION OF THE IMPURITY MODEL

Here we discuss how the parameters of the finite impurity model, Eq. (1), are found so that the model matches the effective medium (the bath) as closely as possible. The impurity Hamiltonian has the form a block matrix

$$\mathbb{H}_{\mathrm{imp}} = \begin{pmatrix} \mathbb{H}_{\mathrm{loc}} & \mathbb{V}_1 & \mathbb{V}_2 & \mathbb{V}_3 & \cdots \\ \mathbb{V}_1^\dagger & \mathbb{H}_{\mathrm{bath}}^{(1)} & 0 & 0 & \cdots \\ \mathbb{V}_2^\dagger & 0 & \mathbb{H}_{\mathrm{bath}}^{(2)} & 0 & \cdots \\ \mathbb{V}_3^\dagger & 0 & 0 & \mathbb{H}_{\mathrm{bath}}^{(3)} & \cdots \\ \vdots & \vdots & \vdots & \vdots & \ddots \end{pmatrix}, \tag{B1}$$

where all blocks are 14×14 square matrices. The local Hamiltonian $\mathbb{H}_{\mathrm{loc}}$ contains a strong spin-orbit coupling which does not commute with the hybridization function that follows the crystal symmetry. Therefore, the problem cannot be simplified to diagonal matrices.

If there is only one $\mathbb{H}_{\mathrm{bath}}$ block, all three matrices $\mathbb{H}_{\mathrm{loc}}$, $\mathbb{H}_{\mathrm{bath}}$, and $\mathbb{V}$ can be determined by comparing the large z asymptotics of the local block of the impurity Green's function,

$$\mathbb{G}_{\mathrm{loc}}(z) = \left[z\mathbb{I} - \mathbb{H}_{\mathrm{loc}} - \sum_i \mathbb{V}_i \left(z\mathbb{I} - \mathbb{H}_{\mathrm{bath}}^{(i)} \right)^{-1} \mathbb{V}_i^\dagger \right]^{-1}, \tag{B2}$$

to the asymptotics of the bath Green's function defined as

$$\mathbb{G}(z) = \left[G_f^{-1}(z) + \Sigma(z)\right]^{-1}. \tag{B3}$$

Here $G_f(z)$ is the $5f$ block of the local Green's function $G(z)$ from Eq. (6). We refer the reader to [32] for details. For larger impurity models, like Eq. (B1), this strategy leads to an unsolvable set of polynomial equations for the 14×14 square matrices. To overcome the problem, we combine two shorter asymptotic expansions, one for the Green's function as before, and one for the hybridization function.

The asymptotic expansion of the local block of the impurity Green's function $\mathbb{G}_{\mathrm{loc}}(z)$ starts as

$$\mathbb{G}_{\mathrm{loc}}(z) = \frac{\mathbb{I}}{z} + \frac{\mathbb{H}_{\mathrm{loc}}}{z^2} + O(z^{-3}), \tag{B4}$$

and the analogous expansion of the hybridization function

$$\Delta_{\mathrm{imp}} = z\mathbb{I} - \mathbb{H}_{\mathrm{loc}} - \mathbb{G}_{\mathrm{loc}}^{-1}(z) \tag{B5}$$

starts as

$$\begin{aligned}\Delta_{\mathrm{imp}} &= \sum_i \mathbb{V}_i \left(z\mathbb{I} - \mathbb{H}_{\mathrm{bath}}^{(i)}\right)^{-1} \mathbb{V}_i^\dagger \\ &= \sum_i \left[\frac{\mathbb{V}_i \mathbb{V}_i^\dagger}{z} + \frac{\mathbb{V}_i\, \mathbb{H}_{\mathrm{bath}}^{(i)}\, \mathbb{V}_i^\dagger}{z^2}\right] + O(z^{-3}).\end{aligned} \tag{B6}$$

From the other side, the bath Green's function, Eq. (B3), reads in the spectral representation as

$$\mathbb{G}(z) = \int \frac{\mathbb{A}(\epsilon)}{z - \epsilon}\, d\epsilon, \tag{B7}$$

where we introduced the spectral density

$$\mathbb{A}(\epsilon) = \frac{\mathbb{G}(\epsilon - \mathrm{i}0) - \mathbb{G}(\epsilon + \mathrm{i}0)}{2\pi\mathrm{i}}. \tag{B8}$$

The asymptotic expansion of the bath Green's function is obtained by expanding the denominator in Eq. (B7),

$$\mathbb{G}(z) = \sum_{n=0}^{\infty} \frac{\mathbb{M}_n}{z^{n+1}}, \quad \mathbb{M}_n = \int \epsilon^n \mathbb{A}(\epsilon)\, d\epsilon, \tag{B9}$$

where $\mathbb{M}_n$ are moments of the spectral density. The spectral density $\mathbb{A}(\epsilon)$ is a hermitian matrix and hence its moments are hermitian matrices as well. We immediately see that

$$\mathbb{H}_{\mathrm{loc}} = \mathbb{M}_1. \tag{B10}$$

The spectral representation of the hybridization function corresponding to $\mathbb{G}(z)$, that is, of $\Delta(z) = z\mathbb{I} - \mathbb{M}_1 - \mathbb{G}^{-1}(z)$, can be written as

$$\Delta(z) = \int \frac{\mathbb{B}(\epsilon)}{z - \epsilon}\, d\epsilon, \tag{B11}$$

where the spectral density is defined as

$$\mathbb{B}(\epsilon) = \frac{\Delta(\epsilon - \mathrm{i}0) - \Delta(\epsilon + \mathrm{i}0)}{2\pi\mathrm{i}}. \tag{B12}$$

Now we split the support of $\mathbb{B}(\epsilon)$ to as many segments as many $\mathbb{H}_{\mathrm{bath}}^{(i)}$ blocks we wish (or can afford) to have,

$$\Delta(z) = \sum_i \Delta_i(z), \text{ where } \Delta_i(z) = \int_{\epsilon_i}^{\epsilon_{i+1}} \frac{\mathbb{B}(\epsilon)}{z - \epsilon}\, d\epsilon \tag{B13}$$

with $\epsilon_i < \epsilon_{i+1}$, and we pair each Δ_i with one summand in Eq. (B6). The splitting can be arbitrary or it can be guided by an insight into the structure of the hybridization function—the individual $\mathbb{H}_{\mathrm{bath}}^{(i)}$ blocks can be aligned with groups of bands. In UGa_2, the hybridization below the Fermi level comes mainly from Ga $4s$ and $4p$ bands, and in the first $\approx$6 eV above the Fermi level it is dominated by U $6d$ bands.

The asymptotic expansion at the individual intervals reads as

$$\Delta_i(z) = \sum_{n=0}^{\infty} \frac{\mathbb{N}_n^{(i)}}{z^{n+1}}, \quad \mathbb{N}_n^{(i)} = \int_{\epsilon_i}^{\epsilon_{i+1}} \epsilon^n \mathbb{B}(\epsilon)\, d\epsilon. \tag{B14}$$

Comparing Eqs. (B6) and (B14), the blocks of $\mathbb{H}_{\mathrm{imp}}$ can be written in terms of the moments $\mathbb{N}_n^{(i)}$ as

$$\mathbb{V}_i = \mathbb{V}_i^\dagger = \sqrt{\mathbb{N}_0^{(i)}}, \tag{B15a}$$

$$\mathbb{H}_{\mathrm{bath}}^{(i)} = \mathbb{V}^{-1} \mathbb{N}_1^{(i)} (\mathbb{V}^\dagger)^{-1}, \tag{B15b}$$

which, together with Eq. (B10), concludes the construction of the impurity model $\mathbb{H}_{\mathrm{imp}}$ from the local Green's function $G(z)$. Optionally, we can diagonalize the blocks $\mathbb{H}_{\mathrm{bath}}^{(i)}$ to make their interpretation more straightforward and to arrive at the form of the impurity model used in Eq. (1). The corresponding transformations are

$$\mathbb{H}_{\mathrm{bath}}^{(i)} \to \mathbb{C}_i^{-1} \mathbb{H}_{\mathrm{bath}}^{(i)} \mathbb{C}_i, \quad \mathbb{V}_i \to \mathbb{V}_i \mathbb{C}_i, \tag{B16}$$

where $\mathbb{C}_i$ are the appropriate unitary matrices and the new $\mathbb{V}_i$ are no longer hermitian. By construction, the eigenvalues of $\mathbb{H}_{\mathrm{bath}}^{(i)}$ are confined to intervals $(\epsilon_i, \epsilon_{i+1})$.

For the purpose of their actual evaluation, the moments are expressed in terms of contour integrals in the complex plane. Using the path segments sketched in Fig. 10, we have

$$\begin{aligned}\mathbb{M}_1 &= \frac{1}{2\pi\mathrm{i}} \left[\int_{-L_-} - \int_{L_+}\right] z\, \mathbb{G}(z)\, dz \\ &= \frac{1}{2\pi\mathrm{i}} \left[\int_{C_-} + \int_{C_+}\right] z\, \mathbb{G}(z)\, dz,\end{aligned} \tag{B17}$$

$$\begin{aligned}\mathbb{N}_n^{(i)} &= \frac{1}{2\pi\mathrm{i}} \left[\int_{-L_-^{(i)}} - \int_{L_+^{(i)}}\right] z^n [z\mathbb{I} - \mathbb{M}_1 - \mathbb{G}^{-1}(z)] dz \\ &= \frac{1}{2\pi\mathrm{i}} \left[\int_{C_-^{(i)}} + \int_{C_+^{(i)}}\right] z^n [z\mathbb{I} - \mathbb{M}_1 - \mathbb{G}^{-1}(z)] dz,\end{aligned} \tag{B18}$$

where the integral over the (dashed blue) circle $C = C_- \cap C_+$ encloses the entire support of $\mathbb{A}(\epsilon)$ and the integrals over the (red) circles $C^{(i)} = C_-^{(i)} \cap C_+^{(i)}$ enclose the intervals $(\epsilon_i, \epsilon_{i+1})$. During the DMFT calculations, the self-energy is thus evaluated along the circles C and $C^{(i)}$, and also along one additional semicircle in the upper half plane to compute the number of electrons in the primitive cell and to adjust the Fermi level. An alternative to the circle C, which serves for evaluation of $\mathbb{H}_{\mathrm{loc}} = \mathbb{M}_1$, is described in Appendix C.

In the DFT+DMFT calculations of UGa_2 discussed in the paper, we used three intervals $(\epsilon_i, \epsilon_{i+1})$, namely, $(-10, 0)$ eV, (0,6) eV, and (6,12) eV. The hybridization above 12 eV was discarded, since our tight-binding Hamiltonians do not accurately represent the original DFT bands that far above the Fermi level (Appendix A).

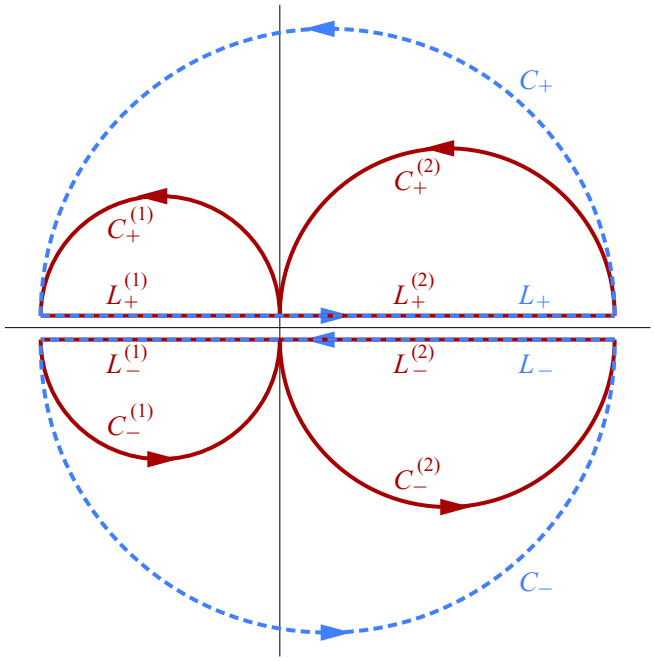

FIG. 10. Contours in the complex plane used for integration of the moments $\mathbb{M}_1$ (dashed blue) and $\mathbb{N}_n^{(i)}$ (red). Line segments are denoted as $L_\pm$, half circles as $C_\pm$.

APPENDIX C: ASYMPTOTICS OF THE BATH GREEN'S FUNCTION AND THE LOCAL HAMILTONIAN

At each k point, the tight-binding Hamiltonian $\hat{H}_\mathbf{k}$ can be divided into four blocks,

$$\hat{H}_\mathbf{k} = \begin{pmatrix} \hat{H}_\mathbf{k}^f & \hat{T}_\mathbf{k} \\ \hat{T}_\mathbf{k}^\dagger & \hat{H}_\mathbf{k}^{spd} \end{pmatrix}, \tag{C1}$$

and the $5f$ block of the lattice Green's function can be written as

$$\hat{G}_\mathbf{k}^f(z) = \left[z\hat{I} - \hat{H}_\mathbf{k}^f - \hat{\Sigma}(z) - \hat{T}_\mathbf{k}\left(z\hat{I} - \hat{H}_\mathbf{k}^{spd}\right)^{-1}\hat{T}_\mathbf{k}^\dagger\right]^{-1}. \tag{C2}$$

Its asymptotic expansion reads as

$$\hat{G}_\mathbf{k}^f(z) = \frac{\hat{I}}{z} + \frac{\hat{H}_\mathbf{k}^f + \hat{\Sigma}(\infty)}{z^2} + O(z^{-3}), \tag{C3}$$

where $\hat{\Sigma}(\infty)$ is the static part of the self-energy, which is the leading term of the expansion $\hat{\Sigma}(z) = \hat{\Sigma}(\infty) + O(z^{-1})$. For the bath Green's function, Eq. (B3), we need only the local element,

$$\begin{aligned} \hat{G}_f(z) &= \frac{1}{N}\sum_\mathbf{k} \hat{G}_\mathbf{k}^f(z) \\ &= \frac{\hat{I}}{z} + \frac{N^{-1}\sum_\mathbf{k} \hat{H}_\mathbf{k}^f + \hat{\Sigma}(\infty)}{z^2} + O(z^{-3}), \end{aligned} \tag{C4}$$

respectively its inverse,

$$\hat{G}_f^{-1}(z) = z\hat{I} - \frac{1}{N}\sum_\mathbf{k} \hat{H}_\mathbf{k}^f - \hat{\Sigma}(\infty) + O(z^{-1}). \tag{C5}$$

TABLE IV. Crystal-field parameters B_{kq}^σ, Eq. (C8e), derived from the LSDA tight-binding Hamiltonian (s, p, d, f model). Spin-restricted parameters B_{kq} computed from Eq. (C8d) are the same as shown in Table I.

	B_{20}	B_{40}	B_{60}	B_{66}
Ferromagnetic solution [001]				
restricted	3.72	0.0061	−0.0043	−0.052
spin ↑	1.75	−0.0024	0.0017	−0.107
spin ↓	5.68	0.0146	−0.0100	0.003
Ferromagnetic solution [210]				
restricted	3.92	0.0262	−0.0011	−0.044
spin ↑	1.54	0.0111	−0.0154	−0.009
spin ↓	6.30	0.0414	0.0133	−0.079

Inserting this expression into the definition of the bath Green's function, Eq. (B3), yields

$$\mathbb{G}(z) = \frac{\hat{I}}{z} + \frac{1}{z^2}\frac{1}{N}\sum_\mathbf{k} \hat{H}_\mathbf{k}^f + O(z^{-1}). \tag{C6}$$

The self-energy cancels out from the first moment of the corresponding spectral density, and the moment thus equals to the local block of the tight-binding Hamiltonian,

$$\mathbb{M}_1 = \frac{1}{N}\sum_\mathbf{k} \hat{H}_\mathbf{k}^f = \mathbb{H}_\mathrm{loc}, \tag{C7}$$

throughout the whole DMFT self-consistency loop.

To extract the individual contributions to the Hamiltonian shown in Eq. (2), we can exploit the orthogonality of operators $\hat{I}$, $\hat{\mathbf{l}}\cdot\hat{\mathbf{s}}$, $\hat{\mathbf{s}}$ and $\hat{O}_{kq}$ as 14×14 matrices. We can write

$$\epsilon_f = \mathrm{Tr}(\mathbb{H}_\mathrm{loc})/14, \tag{C8a}$$

$$\Delta_X^\alpha = \mathrm{Tr}(\hat{s}_\alpha\,\mathbb{H}_\mathrm{loc})/\,\mathrm{Tr}(\hat{s}_\alpha\,\hat{s}_\alpha), \quad \alpha = x, y, z, \tag{C8b}$$

$$\zeta = \mathrm{Tr}(\hat{\mathbf{l}}\cdot\hat{\mathbf{s}}\,\mathbb{H}_\mathrm{loc})/\,\mathrm{Tr}(\hat{\mathbf{l}}\cdot\hat{\mathbf{s}}\,\hat{\mathbf{l}}\cdot\hat{\mathbf{s}}), \tag{C8c}$$

$$B_{kq} = \mathrm{Tr}(\hat{O}_{kq}\,\mathbb{H}_\mathrm{loc})/\,\mathrm{Tr}(\hat{O}_{kq}\hat{O}_{kq}). \tag{C8d}$$

In the case of spin-polarized electronic structure, spin-dependent crystal-field parameters can be introduced as

$$B_{kq}^\sigma = \mathrm{Tr}(\hat{O}_{kq}\hat{P}_\sigma\,\mathbb{H}_\mathrm{loc})/\,\mathrm{Tr}(\hat{O}_{kq}\hat{P}_\sigma\hat{O}_{kq}\hat{P}_\sigma), \tag{C8e}$$

where $\hat{P}_\sigma$ is a projector to spin σ. Since the operator $\hat{O}_{kq}$ is spin-independent, it commutes with $\hat{P}_\sigma$ and we can simplify the denominator as

$$\begin{aligned} \mathrm{Tr}(\hat{O}_{kq}\hat{P}_\sigma\hat{O}_{kq}\hat{P}_\sigma) &= \mathrm{Tr}(\hat{O}_{kq}\hat{O}_{kq}\hat{P}_\sigma\hat{P}_\sigma) \\ &= \mathrm{Tr}(\hat{O}_{kq}\hat{O}_{kq}\hat{P}_\sigma) = \tfrac{1}{2}\,\mathrm{Tr}(\hat{O}_{kq}\hat{O}_{kq}). \end{aligned} \tag{C9}$$

Consequently, the parameters B_{kq} are averages of the spin-dependent parameters B_{kq}^σ,

$$B_{kq} = \frac{1}{2}\sum_\sigma B_{kq}^\sigma. \tag{C10}$$

The spin dependence of the crystal-field parameters derived from the LSDA band structure is substantial, which is illustrated in Table IV. Note that we do not attempt to remove the $5f$ self-interaction from the crystal-field potential [44,45].

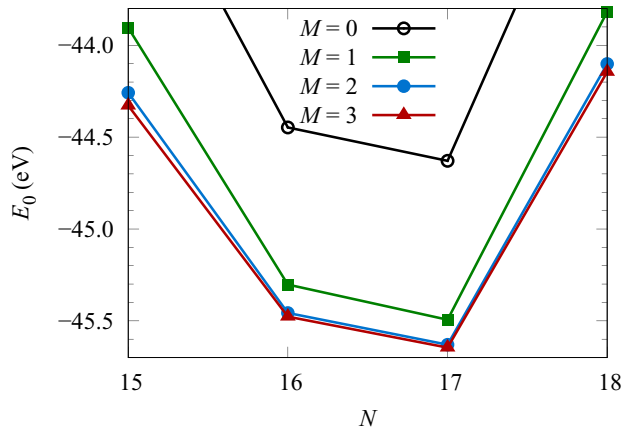

FIG. 11. The ground-state energy E_0 of the impurity model at different fillings N computed for increasing size of the many-body basis characterized by the cutoff M.

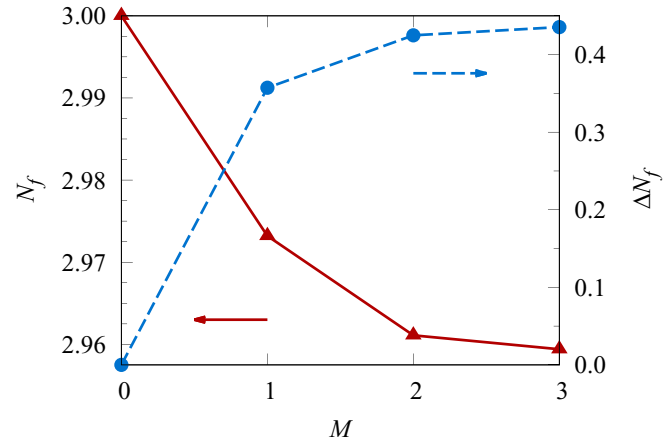

FIG. 12. Convergence of the $5f$ occupation number N_f (red triangles, left axis) and its fluctuation ΔN_f (blue circles, right axis) with respect to the basis-set cutoff M.

Nevertheless, the spin dependence would not disappear even if we did [45].

APPENDIX D: CONVERGENCE OF THE IMPURITY-MODEL SOLUTION WITH THE SIZE OF THE MANY-BODY BASIS

As indicated in Sec. II A, we cannot diagonalize the impurity model in the complete Fock space, only in reduced subspaces $\mathcal{H}_N^{(M)}$, defined in Eq. (5), where N is the number of electrons in the model (its filling) and M is a cutoff parameter. Analyzing the convergence of the complete DMFT solution with respect to M is computationally very demanding. Hence, we limit this Appendix to selected intermediate quantities, evaluation of which does not involve computing the self-energy. In particular, we diagonalize the auxiliary impurity model corresponding to the [210] ferromagnetic LDA+DMFT solution, obtained for $\Delta_{fd} = 35$ meV and presented in Sec. III, for different settings of the cutoff parameter M. The crudest approximation is $M = 0$ that does not allow any hops of electrons between the $5f$ shell and the bath, and thus corresponds to the Hubbard-I approximation. The best approximation we consider is $M = 3$, one step better than the setting employed in the main text.

Figure 11 shows the M dependence of the ground-state energy E_0 for fillings N around the overall grand canonical ground state which is located at $N = 17$. The differences between the $M = 2$ and $M = 3$ basis sets are very small (less than 70 meV), which indicates that $M = 2$ is indeed a sensible choice. The differences are even smaller (less than 30 meV) for energy gaps $E_0(N \pm 1) - E_0(N)$ that determine the positions of the main peaks in the valence-band spectra like those plotted in Fig. 8.

Furthermore, we present the $5f$ occupation number $N_f = \mathrm{Tr}(\hat{N}_f\,\hat{\rho})$, where $\hat{\rho}$ is the grand canonical density matrix of the impurity model, together with its fluctuation

$$\Delta N_f = \sqrt{\mathrm{Tr}\left(\hat{N}_f^2\,\hat{\rho}\right) - N_f^2} \tag{D1}$$

as functions of the cutoff M in Fig. 12. Both these quantities again change very little when M is increased from $M = 2$ to $M = 3$, which represents another reassurance that $M = 2$ is good enough.

Note that N_f should be the same number as n_f defined in Eq. (8) and listed in Table II, which follows from the DMFT embedding condition. In our DMFT calculations, they are not the same, N_f is approximately 0.2 larger than n_f, which is a consequence of the approximate finite impurity model (discrete bath) being used instead of the exact infinite impurity model (continuous bath). This is roughly the same discrepancy as we observed earlier when we applied this method to the ferromagnetic nickel [46]. In principle, the situation could be improved by adding more bath orbitals, but in practice, it is computationally prohibitive at present.

[1] K. T. Moore and G. van der Laan, Nature of the $5f$ states in actinide metals, Rev. Mod. Phys. **81**, 235 (2009).

[2] H. H. Hill, in *Plutonium 1970 and other Actinides*, edited by W. N. Miner (The Metallurgical Society of the AIME, New York, 1970), p. 2.

[3] A. V. Andreev, K. P. Belov, A. V. Deryagin, Z. A. Kazei, R. Z. Levitin, A. Meňovský, Yu. F. Popov, and V. I. Silant'ev, Crystal structure, and magnetic and magnetoelastic properties of UGa_2, Sov. Phys. JETP **48**, 1187 (1978).

[4] A. V. Kolomiets, J.-C. Griveau, J. Prchal, A. V. Andreev, and L. Havela, Variations of magnetic properties of UGa_2 under pressure, Phys. Rev. B **91**, 064405 (2015).

[5] A. C. Lawson, A. Williams, J. L. Smith, P. A. Seeger, J. A. Goldstone, J. A. O'Rourke, and Z. Fisk, Magnetic neutron diffraction study of UGa_3 and UGa_2, J. Magn. Magn. Mater. **50**, 83 (1985).

[6] R. Ballou, A. V. Deriagin, F. Givord, R. Lemaire, R. Z. Levitin, and F. Tasset, U^{4+} form factor in UGa_2, J. Phys. Colloques **43**, C7–279 (1982).

[7] J.-M. Fournier and R. Troc, in *Handbook on the Physics and Chemistry of the Actinides*, edited by A. Freeman and G. Lander (North Holland, Amsterdam, 1985), Vol. 2, p. 35.

[8] R. J. Radwański and N. H. Kim-Ngan, The crystal-field and exchange interactions in UGa_2, J. Magn. Magn. Mater. **140–144**, 1373 (1995).

[9] T. Honma, Y. Inada, R. Settai, S. Araki, Y. Tokiwa, T. Takeuchi, H. Sugawara, H. Sato, K. Kuwahara, M. Yokoyama, H. Amitsuka, T. Sakakibara, E. Yamamoto, Y. Haga, A. Nakamura, H. Harima, H. Yamagami, and Y. Ōnuki, Magnetic and Fermi surface properties of the ferromagnetic compound UGa_2, J. Phys. Soc. Jpn. **69**, 2647 (2000).

[10] Y. Fujimaki, K. Satoh, and Y. Ōnuki, Superconductivity in $LaGa_2$, J. Phys. Soc. Jpn. **61**, 395 (1992).

[11] T. Gouder, L. Havela, M. Diviš, J. Rebizant, P. M. Oppeneer, and M. Richter, Surface electronic structure of UGa_x films, J. Alloys Compd. **314**, 7 (2001).

[12] S.-i. Fujimori, M. Kobata, Y. Takeda, T. Okane, Y. Saitoh, A. Fujimori, H. Yamagami, Y. Haga, E. Yamamoto, and Y. Ōnuki, Manifestation of electron correlation effect in $5f$ states of uranium compounds revealed by $4d$–$5f$ resonant photoelectron spectroscopy, Phys. Rev. B **99**, 035109 (2019).

[13] A. V. Kolomiets, M. Paukov, J. Valenta, B. Chatterjee, A. V. Andreev, K. Kvashnina, F. Wilhelm, A. Rogalev, D. Drozdenko, P. Minarik, J. Kolorenč, M. Richter, and L. Havela, $5f$ states in UGa_2 probed by x-ray spectroscopies (unpublished, 2021).

[14] M. Diviš, M. Richter, H. Eschrig, and L. Steinbeck, *Ab initio* electronic structure, magnetism, and magnetocrystalline anisotropy of UGa_2, Phys. Rev. B **53**, 9658 (1996).

[15] B. Chatterjee and J. Kolorenč, Magnetism and magnetic anisotropy in UGa_2, MRS Adv. **5**, 2639 (2020).

[16] V. I. Anisimov, F. Aryasetiawan, and A. I. Lichtenstein, First-principles calculations of the electronic structure and spectra of strongly correlated systems: the LDA + U method, J. Phys.: Condens. Matter **9**, 767 (1997).

[17] M.-T. Suzuki, N. Magnani, and P. M. Oppeneer, Microscopic theory of the insulating electronic ground states of the actinide dioxides AnO_2 (An = U, Np, Pu, Am, and Cm), Phys. Rev. B **88**, 195146 (2013).

[18] R. Qiu, B. Ao, and L. Huang, Effective Coulomb interaction in actinides from linear response approach, Comp. Mater. Sci. **171**, 109270 (2020).

[19] V. N. Antonov, B. N. Harmon, and A. N. Yaresko, Electronic structure and magneto-optical Kerr effect in UGa_2, J. Appl. Phys. **94**, 7240 (2003).

[20] A. I. Lichtenstein and M. I. Katsnelson, *Ab initio* calculations of quasiparticle band structure in correlated systems: LDA++ approach, Phys. Rev. B **57**, 6884 (1998).

[21] G. Kotliar, S. Y. Savrasov, K. Haule, V. S. Oudovenko, O. Parcollet, and C. A. Marianetti, Electronic structure calculations with dynamical mean-field theory, Rev. Mod. Phys. **78**, 865 (2006).

[22] A. Georges, G. Kotliar, W. Krauth, and M. J. Rozenberg, Dynamical mean-field theory of strongly correlated fermion systems and the limit of infinite dimensions, Rev. Mod. Phys. **68**, 13 (1996).

[23] M. I. Katsnelson and A. I. Lichtenstein, Electronic structure and magnetic properties of correlated metals, Eur. Phys. J. B **30**, 9 (2002).

[24] P. Blaha, K. Schwarz, F. Tran, R. Laskowski, G. K. H. Madsen, and L. D. Marks, WIEN2k: An APW+lo program for calculating the properties of solids, J. Chem. Phys. **152**, 074101 (2020).

[25] D. D. Koelling and B. N. Harmon, A technique for relativistic spin-polarised calculations, J. Phys. C: Solid State Phys. **10**, 3107 (1977).

[26] J. Kuneš, R. Arita, P. Wissgott, A. Toschi, H. Ikeda, and K. Held, Wien2wannier: From linearized augmented plane waves to maximally localized Wannier functions, Comput. Phys. Commun. **181**, 1888 (2010).

[27] A. A. Mostofi, J. R. Yates, Y.-S. Lee, I. Souza, D. Vanderbilt, and N. Marzari, wannier90: A tool for obtaining maximally-localised Wannier functions, Comput. Phys. Commun. **178**, 685 (2008).

[28] R. D. Cowan, *The Theory of Atomic Structure and Spectra* (University of California Press, Berkeley, 1981).

[29] H. Ogasawara, A. Kotani, and B. T. Thole, Calculation of magnetic x-ray dichroism in $4d$ and $5d$ absorption spectra of actinides, Phys. Rev. B **44**, 2169 (1991).

[30] H.-D. Meyer and S. Pal, A band-Lanczos method for computing matrix elements of a resolvent, J. Chem. Phys. **91**, 6195 (1989).

[31] A. Liebsch and H. Ishida, Temperature and bath size in exact diagonalization dynamical mean field theory, J. Phys.: Condens. Matter **24**, 053201 (2012).

[32] J. Kolorenč, A. B. Shick, and A. I. Lichtenstein, Electronic structure and core-level spectra of light actinide dioxides in the dynamical mean-field theory, Phys. Rev. B **92**, 085125 (2015).

[33] O. Gunnarsson and K. Schönhammer, Electron spectroscopies for Ce compounds in the impurity model, Phys. Rev. B **28**, 4315 (1983).

[34] L. V. Pourovskii, G. Kotliar, M. I. Katsnelson, and A. I. Lichtenstein, Dynamical mean-field theory investigation of specific heat and electronic structure of α- and δ-plutonium, Phys. Rev. B **75**, 235107 (2007).

[35] L. Peters, I. Di Marco, P. Thunström, M. I. Katsnelson, A. Kirilyuk, and O. Eriksson, Treatment of $4f$ states of the rare earths: The case study of TbN, Phys. Rev. B **89**, 205109 (2014).

[36] A. Shick and A. Lichtenstein, Electronic structure and magnetic properties of Dy adatom on Ir surface, J. Magn. Magn. Mater. **454**, 61 (2018).

[37] M. S. S. Brooks and B. Johansson, Exchange integral matrices and cohesive energies of transition metal atoms, J. Phys. F: Met. Phys. **13**, L197 (1983).

[38] I. V. Solovyev, P. H. Dederichs, and V. I. Anisimov, Corrected atomic limit in the local-density approximation and the electronic structure of d impurities in Rb, Phys. Rev. B **50**, 16861 (1994).

[39] B. Amadon, F. Lechermann, A. Georges, F. Jollet, T. O. Wehling, and A. I. Lichtenstein, Plane-wave based electronic structure calculations for correlated materials using dynamical mean-field theory and projected local orbitals, Phys. Rev. B **77**, 205112 (2008).

[40] L. Havela, S. Mašková, J. Kolorenč, E. Colineau, J.-C. Griveau, and R. Eloirdi, Electronic properties of $Pu_{19}Os$ simulating β-Pu: the strongly correlated Pu phase, J. Phys.: Condens. Matter **30**, 085601 (2018).

[41] S.-i. Fujimori (private communication, 2020).

[42] J. Yeh and I. Lindau, Atomic subshell photoionization cross sections and asymmetry parameters: $1 \leqslant Z \leqslant 103$, At. Data Nucl. Data Tables. **32**, 1 (1985).

[43] I. Souza, N. Marzari, and D. Vanderbilt, Maximally localized Wannier functions for entangled energy bands, Phys. Rev. B **65**, 035109 (2001).

[44] P. Novák, K. Knížek, and J. Kuneš, Crystal field parameters with Wannier functions: Application to rare-earth aluminates, Phys. Rev. B **87**, 205139 (2013).

[45] P. Delange, S. Biermann, T. Miyake, and L. Pourovskii, Crystal-field splittings in rare-earth-based hard magnets: An ab initio approach, Phys. Rev. B **96**, 155132 (2017).

[46] J. Kolorenč, A. I. Poteryaev, and A. I. Lichtenstein, Valence-band satellite in ferromagnetic nickel: LDA+DMFT study with exact diagonalization, Phys. Rev. B **85**, 235136 (2012).